



The Combined Effects of Two-body Relaxation Processes and the Eccentric Kozai–Lidov Mechanism on the Extreme-mass-ratio Inspirals Rate

Smadar Naoz^{1,2} , Sanaea C. Rose^{1,2} , Erez Michaely^{1,2} , Denyz Melchor^{1,2} , Enrico Ramirez-Ruiz³ ,
Brenna Mockler³ , and Jeremy D. Schnittman^{4,5}

¹ Department of Physics and Astronomy, University of California, Los Angeles, CA 90095, USA

² Mani L. Bhaumik Institute for Theoretical Physics, Department of Physics and Astronomy, UCLA, Los Angeles, CA 90095, USA

³ Department of Astronomy and Astrophysics, University of California, Santa Cruz, CA 95064, USA

⁴ NASA Goddard Space Flight Center, Greenbelt, MD 20771, USA

⁵ Maryland Joint Space-Science Institute, College Park, MD 20742, USA

Received 2021 December 10; revised 2022 February 11; accepted 2022 February 22; published 2022 March 8

Abstract

Gravitational wave (GW) emissions from extreme-mass-ratio inspirals (EMRIs) are promising sources for low-frequency GW detectors. They result from a compact object, such as a stellar-mass black hole (BH), captured by a supermassive BH (SMBH). Several physical processes have been proposed to form EMRIs. In particular, weak two-body interactions over a long timescale (i.e., relaxation processes) have been proposed as a likely mechanism to drive the BH orbit to high eccentricity. Consequently, it is captured by the SMBH and becomes an EMRI. Here we demonstrate that EMRIs are naturally formed in SMBH binaries. Gravitational perturbations from an SMBH companion, known as the eccentric Kozai–Lidov (EKL) mechanism, combined with relaxation processes, yield a significantly more enhanced rate than any of these processes operating alone. Because EKL is sensitive to the orbital configuration, two-body relaxation can alter the orbital parameters, rendering the system in a more EKL-favorable regime. As SMBH binaries are expected to be prevalent in the universe, this process predicts a substantially high EMRI rate.

Unified Astronomy Thesaurus concepts: [Astrophysical black holes \(98\)](#); [Supermassive black holes \(1663\)](#); [Gravitational waves \(678\)](#); [Gravitational wave astronomy \(675\)](#); [Galaxy nuclei \(609\)](#); [Galaxy structure \(622\)](#); [Galactic center \(565\)](#)

1. Introduction

Extreme-mass-ratio inspirals (EMRIs) arise from the capture of a stellar-mass compact object by a supermassive black hole (SMBH). The gravitational wave (GW) emission from such a system is expected to be at the millihertz band, thus a promising signal for the Laser Interferometer Space Antenna (LISA), as well as other millihertz detectors, such as TianQin (e.g., Amaro-Seoane et al. 2017; Baker et al. 2019; Robson et al. 2019b; Mei et al. 2020). Thus, the rate estimation of EMRIs is of high importance for these detections.

EMRI rate estimation studies often focused on the “loss cone” mechanism, in which stellar-mass black holes (BHs) undergo weak two-body scatterings and over time are able to reach high eccentricities (e.g., Hopman & Alexander 2005; Aharon & Perets 2016; Amaro-Seoane 2018; Sari & Fragione 2019). Additionally, weak two-body interactions can also lead to mass segregation if the BH is more massive than the surrounding population of stars (e.g., Hopman & Alexander 2006; Alexander & Hopman 2009; Preto & Amaro-Seoane 2010; Amaro-Seoane & Preto 2011; Chen & Han 2018). Other physical processes have also been suggested to contribute to the formation of EMRIs, for example, the tidal separation of BH binaries by SMBHs was suggested to form a low-eccentricity LISA event (e.g., Miller et al. 2005; Raveh & Perets 2021, the latter also include the effects of mass segregation). Furthermore, accretion disks around SMBHs in

active galactic nuclei (AGNs) have been suggested to further increase the EMRI rate (e.g., Pan & Yang 2021).

Of particular interest here is the formation of EMRIs in SMBH binaries. Thanks to the hierarchical nature of galaxy formation, and because almost every galaxy hosts an SMBH at its center, SMBH binaries are expected to be a common phenomenon (e.g., Di Matteo et al. 2005; Hopkins et al. 2006; Robertson et al. 2006; Callegari et al. 2009; Li et al. 2020). Observations of AGN pairs, which are typically a few kiloparsecs (and more) apart, suggest that these configurations may lead to the formation of SMBH binaries with parsec to subparsec separations (e.g., Komossa et al. 2003; Bianchi et al. 2008; Comerford et al. 2009, 2018; Green et al. 2010; Liu et al. 2010; Smith et al. 2010; Stemo et al. 2021). Moreover, observations of SMBH binaries on wide orbits, as well as some subparsec candidates, seem to support this idea (e.g., Sillanpaa et al. 1988; Rodriguez et al. 2006; Komossa et al. 2008; Bogdanović et al. 2009; Boroson & Lauer 2009; Dotti et al. 2009; Batcheldor et al. 2010; Deane et al. 2014; Runnoe et al. 2017; Pesce et al. 2018). Lastly, a combination of theoretical and observational studies suggested that our own galactic center may also host a companion (albeit a small one) (e.g., Hansen & Milosavljević 2003; Maillard et al. 2004; Gürkan & Rasio 2005; Gualandris & Merritt 2009; Chen & Liu 2013; Fragione et al. 2020; GRAVITY Collaboration et al. 2020; Generozov & Madigan 2020; Naoz et al. 2020; Zheng et al. 2020).

An SMBH companion gravitationally perturbs the orbit of a stellar-mass BH via the eccentric Kozai–Lidov mechanism (EKL; e.g., Kozai 1962; Lidov 1962; Naoz 2016, see latter for review). These perturbations can result in extreme eccentricities



Original content from this work may be used under the terms of the [Creative Commons Attribution 4.0 licence](#). Any further distribution of this work must maintain attribution to the author(s) and the title of the work, journal citation and DOI.

(e.g., Li et al. 2014a, 2014b; Naoz & Silk 2014), which can lead to the formation of EMRIs (e.g., Bode & Wegg 2014; Haster et al. 2016). A similar process is often considered for the production of tidal disruption events (e.g., Chen et al. 2008, 2009, 2011; Chen & Liu 2013; Li et al. 2015; B. Mockler et al. 2022, in preparation).

The EKL approach often ignores collective dynamical interaction because these interactions operate on much longer timescales. In particular, relaxation by gravitational encounters typically takes place on such long timescales, compared to other physical processes (see below), and thus often is ignored when considering EKL processes. Here we show that the combined effect of EKL and relaxation processes enhances the EMRI formation efficiency more than any of these processes operating alone. Furthermore, the two-body relaxation processes overcome the general relativistic precession that suppresses EKL resonances. We begin by describing the methodology of the system in Section 2. We then consider an example system and present proof-of-concept Monte Carlo results of a fiducial system in Section 3. We show that this mechanism can potentially result in a much higher EMRI rate in Section 4, and we offer our discussion in Section 5.

2. Methodology and System Setup

2.1. Fiducial System

We consider a system of an SMBH binary with masses m_1 and m_2 , and orbital period P_{bin} . Surrounding the primary m_1 is a sphere of compact objects at distance r , and masses m_* , where for simplicity we assume the same masses.⁶ Note that here $m_1 < m_2$. We emphasize that the physical processes described below are scalable beyond the fiducial system adopted here. In particular, we expect that two-body relaxation will play a critical role in the EKL process of a population of stars and a wide range of compact object masses surrounding SMBHs. The stellar-mass BH's (m_*) density profile $\rho(r)$ is calibrated by the M - σ relation (Tremaine et al. 2002):

$$\rho(r) = \frac{3 - \alpha}{2\pi} \frac{m_1}{r_*^3} \left(\frac{G\sqrt{m_1 M_0}}{\sigma_0^2 r_*} \right)^{-3+\alpha}, \quad (1)$$

where $M_0 = 10^8 M_\odot$ and $\sigma_0 = 200 \text{ km s}^{-1}$ are scaling factors. Below we adopt a Bahcall & Wolf (1976) profile, i.e., $\alpha = 1.75$. Note that these values have been slightly modified recently (e.g., McConnell & Ma 2013; van den Bosch 2016). However, it does not affect the underlying physical processes described below and only may slightly change the relaxation timescale (see Section 2.4).

Each BH (m_*) undergoes eccentricity and inclination excitations due to the faraway SMBH companion (m_2) according to the EKL mechanism. Additionally, general relativity effects induce precession and can also circularize and shrink the orbit through GW emission. Finally, collective relaxation interactions with the sea of objects in the sphere of influence tend to change the angular momentum and energy of the orbit by an order of themselves over long timescales. Below we specify these different physical processes and outline the methodology of including them in our analysis.

⁶ Different populations may result in slightly different density profiles; see Aharon & Perets (2016).

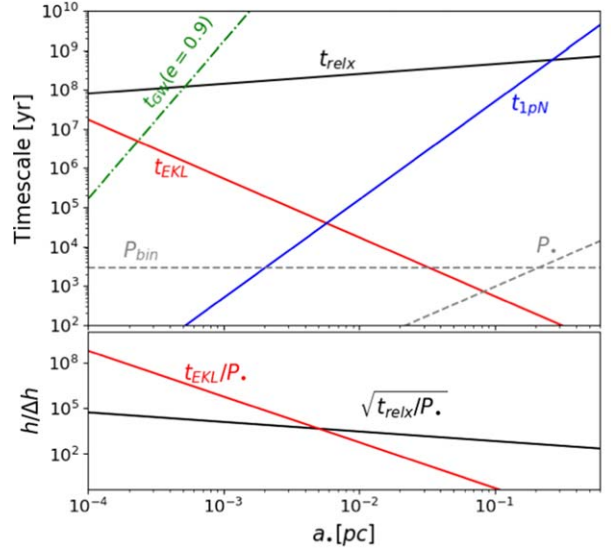
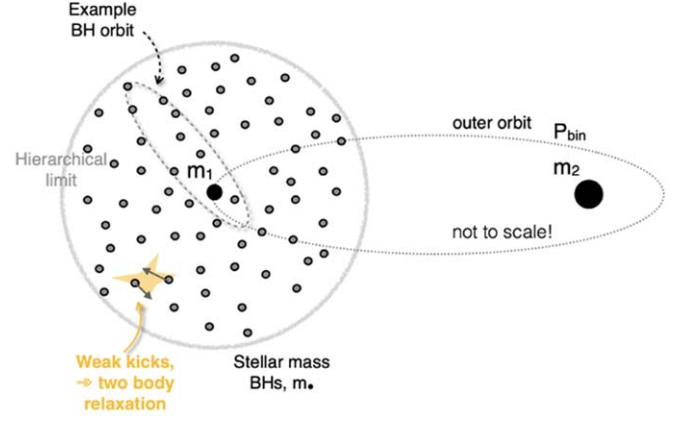


Figure 1. Top panel: an illustration of the system. Middle panel: an example of the timescales in the system. We consider an SMBH of mass $m_1 = 10^7 M_\odot$ with a population of $10 M_\odot$ BHs. The period of the BHs around m_1 is shown by the dashed line (labeled P_*), and the associated 1pN precession is shown as the blue line, labeled t_{1pN} , according to Equation (3). The weak interactions between the BHs result in the two-body relaxation timescale (see Equation (5)), shown by the black line. We also consider an SMBH companion with $m_2 = 10^9 M_\odot$, at 1 pc separation (note that $m_1 < m_2$ in this configuration). The period of the SMBH binary is shown as the dashed line labeled P_{bin} , and the resulting EKL timescale is the red line labeled t_{EKL} ; see Equation (2). Bottom panel: proposed alternative to quantify the relative importance of the two-body relaxation processes compared to EKL. We consider $h/\Delta h$ (the relative change in angular momentum “ h ”), due to both two-body relaxation and EKL, where $h/\Delta h_{\text{relx}} \sim \sqrt{t_{\text{relx}}/P_*}$ for two-body processes and $h/\Delta h_{\text{EKL}} \sim t_{\text{EKL}}/P_*$ for EKL. See text (Section 3.1) for more details.

2.2. Three-body Secular Analysis

We solve the hierarchical three-body secular equations up to the octupole level of approximation (see for a complete set of equations Naoz et al. 2013a). The timescale of the lowest order of approximation, namely the quadrupole, is (e.g., Antognini 2015) estimated as

$$t_{\text{EKL}} \sim \frac{16}{30\pi} \frac{m_1 + m_*}{m_2} \frac{P_{\text{bin}}^2}{P_*} (1 - e_{\text{bin}}^2)^{3/2}, \quad (2)$$

where P_{bin} and e_{bin} are the period and eccentricity of the SMBH binary, respectively, and P_* is the period of the stellar-mass BH around m_1 . We show this timescale in Figure 1.

2.3. General Relativity and Gravitational Waves

The first post-Newtonian (pN) effects induced by m_1 cause m_* to precess on a characteristic timescale

$$t_{\text{pN}} \sim \frac{Pc^2a_*(1 - e_*^2)}{6\pi G(m_1 + m_*)}, \quad (3)$$

where c is the speed of light. When this timescale is shorter than the quadrupole timescale from Equation (2) eccentricity excitations are typically suppressed (e.g., Ford et al. 2000; Naoz et al. 2013b; Will & Maitra 2017; Lim & Rodriguez 2020). However, when these two timescales are similar, the precession may excite eccentricities and even retrigger the EKL behavior of extreme eccentricity and inclination flips (Naoz et al. 2013b) by destabilizing the quadrupole-level resonance (see, Hansen & Naoz 2020). The timescales of m_* for a fiducial system are shown in Figure 1.

We include in our calculations both the first pN effects from the primary m_1 and the secondary m_2 . As mentioned in Naoz & Silk (2014) and Li et al. (2015), we choose to focus on the BHs around the less massive SMBH to minimize the part of the parameter space in which first pN precession suppresses the EKL's eccentricity excitations. As we highlight below, in the presence of two-body relaxation this suppression is minimized.

In addition to 1pN precession, we also include the shrinking and circularization of the stellar-mass BH orbit due to gravitational wave emission following Peters & Mathews (1963). The characteristic timescale to merge an EMRI is

$$t_{\text{GW}} \sim 5.8 \times 10^9 \text{ yr} \left(\frac{m_1}{10^6 M_\odot} \right)^{-2} \left(\frac{m_*}{10 M_\odot} \right)^{-1} \left(\frac{a_*}{10^{-4} \text{ pc}} \right)^4 \times f(e_*)(1 - e_*^2)^{7/2}, \quad (4)$$

where $f(e_*)$ is a function of e_* and for all values of e_* is between 0.979 and 1.81, (Blaes et al. 2002). We show this timescale for our fiducial system in Figure 1 for $e_* = 0.9$.

2.4. Two-body Relaxation

Scattering relaxation interactions of a target BH with the sea of objects are modeled by considering the two-body relaxation timescale (e.g., Binney & Tremaine 2008)

$$t_{\text{relx}} = 0.34 \frac{\sigma^3}{G^2 \rho \langle m_{\text{scat}} \rangle \ln \Lambda}, \quad (5)$$

where $\langle m_{\text{scat}} \rangle$ is the mass of the average scatterer, σ is the velocity dispersion of BHs around the SMBH:

$$\sigma = \frac{Gm_1}{r_*(1 + \alpha)}, \quad (6)$$

where α is the slope of the density profile. The Coulomb logarithm is

$$\ln \Lambda = \frac{r_* \sigma^2}{2G \langle m_{\text{scat}} \rangle}. \quad (7)$$

For simplicity, we adopt $\langle m_{\text{scat}} \rangle \approx m_*$. However, if $\langle m_{\text{scat}} \rangle \ll m_*$, mass segregation may migrate the BHs inwards.

The relaxation time from Equation (5) is the timescale for a change of energy of the stellar-mass BH around the SMBH m_1 by an order of its orbital energy or a change in angular

momentum by an order of its circular angular momentum. We show the relaxation timescale in Figure 1 (solid black line on top), which for a large part of the parameter space is much larger than the EKL timescale. As mentioned, this motivated many studies to ignore the contribution of two-body relaxation when considering EKL effects.

The typical change in the BH's velocity $v_* = \sqrt{Gm_1(2/r_* - 1/a_*)}$ due to one encounter is

$$\Delta v = v_* \sqrt{\frac{P}{t_{\text{relx}}}}. \quad (8)$$

We model this change as a random walk, applying a single isotropically oriented kick to the BH velocity once per orbit around the SMBH. Each directional component of this 3D kick is drawn from a Gaussian distribution with a zero average and a standard deviation of $\Delta v/\sqrt{3}$ (see Bradnick et al. 2017 for a similar approach for binaries around a single SMBH). We assume that the kick is instantaneous at some random phase of the BH's orbit,

$$r_* = \frac{a_*(1 - e_*^2)}{1 + e_* \cos f_*}, \quad (9)$$

where f_* is the true anomaly.⁷ Thus, the vector \mathbf{r}_* in the invariable plane⁸ can be considered constant during the encounter. See Appendix A for the full set of two-body relaxation equations.

3. Dynamical Evolution

3.1. Example System and Revisiting the Timescale Argument

The EKL mechanism tends to excite high eccentricities and inclination. However, only about 30% of the parameter space in the aforementioned configuration is available to reach the extreme eccentricities needed to drive an object into the BH and cross its Schwarzschild radius (e.g., Naoz & Silk 2014; Li et al. 2015; Naoz et al. 2019). As an example, we consider in Figure 2 a system whose EKL eccentricity excitations do not result in values sufficient to cross the SMBH's Schwarzschild radius (gray lines in both columns). For this system, the EKL timescale ($t_{\text{EKL}} \sim 1.4 \times 10^4$ yr) is shorter than the general relativity (GR) precession timescale ($t_{\text{1pN}} \sim 6 \times 10^6$ yr).

However, as can be seen in Figure 2, left column, a two-body relaxation process combined with EKL results in aggravated EKL eccentricity and inclination excitations. We note that we include GR precession for the inner and outer orbits. The former suppresses the EKL eccentricity excitations when two-body relaxation is not included (gray lines). However, in this example, we do not include GW emission. To avoid clutter, GW is included in the Monte Carlo analysis below. In this example (Figure 2, left column), we consider a BHH population with a Bahcall & Wolf (1976) distribution (i.e., $\alpha = 7/4$). The two-body relaxation timescale from Equation (5) is $t_{\text{relx}} \approx 3.5 \times 10^8$ yr, well above the EKL timescale (see also Figure 1; for this case, it is about four orders of magnitude larger). By definition, over the ≈ 1.5 Myr

⁷ Note that we choose the eccentric anomaly from a uniform distribution and find the true anomaly from there.

⁸ Note that the system evolves due to EKL and thus we need to project the separation vector on the invariable plane. For a similar analysis, see, e.g., Lu & Naoz (2019).

run, the relaxation timescale is insufficient to change the angular momentum by an order of itself (because the timescale is shorter than t_{relx} in this case). However, the combined effect of two-body relaxation and EKL results in higher eccentricity and inclination amplitude modulations.

In fact, the eccentricity excitations were large enough to drive this stellar-mass BH onto the SMBH, thus forming an EMRI. The higher eccentricity values reached are correlated with the BH semimajor axis slightly drifting to higher values, due to two-body relaxation, thus getting closer to the secondary SMBH (m_2). This process yields a shorter EKL timescale (recall the Equation (2) dependency on the inner orbital period). Furthermore, as the inner orbit gets closer to the secondary SMBH, the octupole level of the approximation dominates more. This behavior is expressed by the prefactor of the octupole-level Hamiltonian ϵ (e.g., Lithwick & Naoz 2011):

$$\epsilon = \frac{a \cdot e_{\text{bin}}}{a_{\text{bin}} (1 - e_{\text{bin}}^2)}. \quad (10)$$

Thus, as a increases, so does ϵ , which excites the eccentricity of the BH toward larger values (e.g., Li et al. 2014a, 2014b).

The obvious questions from this result are why these diffusion processes create such a large effect, and will they always happen regardless of the value of t_{relx} . The answers to both of these questions can be understood by examining Equation (8), which suggests that $h/\Delta h|_{\text{relx}} \sim \sqrt{t_{\text{relx}}}$, where h is the angular momentum and Δh is the change of the angular momentum due to a small kick over the particle orbit around m_1 . However, the angular momentum changes due to the EKL are $h/\Delta h|_{\text{EKL}} \sim t_{\text{EKL}}$ (e.g., Naoz et al. 2013a). Thus, effectively, we should compare $\sqrt{t_{\text{relx}}/P}$ to t_{EKL}/P . We show this comparison in Figure 1, bottom panel, where we compare $h/\Delta h$, due to the different processes. Using this picture, it is clearer that two-body relaxation is relevant to a large part of the parameter space.

In the example depicted in the left column of Figure 2, even though $h/\Delta h|_{\text{relx}} > h/\Delta h|_{\text{EKL}}$, it is only by a factor of 20, which yields this cumulative effect (examining the bottom panel in Figure 1 helps clarify the comparison between the two effects). About an order-of-magnitude difference can still lead to a significant cumulative effect. This behavior is similar to the way that GR precession destabilizes the quadrupole resonance, even when its timescale is much longer than the quadrupole level (e.g., Naoz et al. 2017; Hansen & Naoz 2020). We note of course that for this system, two-body relaxation effects would have eventually changed the energy and angular momentum of the orbit by an order of themselves, regardless of EKL. However, this does not guarantee an orbit that will plunge onto m_1 . In our case, we have adopted a Bahcall & Wolf distribution (1976), i.e., $\alpha = 7/4$, which results in zero net flux, thus, the BHs are expected to undergo diffusion but not preferentially migrate.

We emphasize that the two-body relaxation effect on the orbital configuration is indeed small compared to the long-term EKL eccentricity excitation. This is highlighted in Figure 2 for the two-body relaxation-only case (red lines), which does not excite the eccentricity to any meaningfully high values during the simulation runtime. Instead, the BH simply undergoes diffusion in its energy and angular momentum. However, because the EKL is sensitive to the orbital configuration, the diffusion in energy and angular momentum due to two-body relaxation can still contribute to large effects on the BH orbit. If

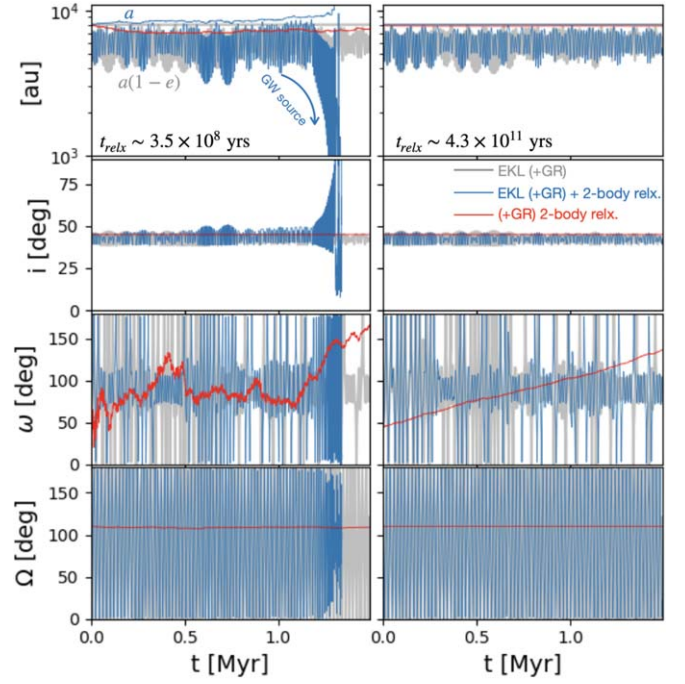


Figure 2. Time evolution of an example system in the presence of different physical processes. We show, from top to bottom, a stellar-mass black hole separation around an SMBH, inclination with respect to the outer perturber, the argument of periaapsis, and longitude of ascending nodes. Left side: We consider a stellar-mass black hole ($m_* = 10 M_\odot$) orbiting an SMBH ($m_1 = 10^7 M_\odot$), at $a_* = 8000$ au, initially with $e_* = 0.02$, $\omega_* = 45^\circ$, $\Omega_* = 110^\circ$. We also consider a population of stellar-mass black holes around m_1 , following a Bahcall & Wolf (1976) profile (i.e., $\alpha = 1.75$). We normalize the density profile according to the m - σ relation, (see Equation (1)), which results in a two-body relaxation timescale of $t_{\text{relx}} \sim 3.5 \times 10^8$ yr. We show the resulting orbital evolution of the stellar-mass BH in the thick red line. We also introduce a binary SMBH with mass $m_2 = 10^9 M_\odot$ set on 1 pc separation, with an eccentricity of $e_{\text{bin}} = 0.7$. The evolution that includes both the two-body relaxation and the EKL from the outer orbit (as well as the GR precession on the inner orbit) is shown by the thin blue line. As depicted, this system reached extreme eccentricities induced by a combination of two-body relaxation and EKL and pushed toward the SMBH, producing a GW source. We also consider the case in which we ignore the contribution of two-body relaxation processes and consider only the EKL (+GR) in light gray. This system never reached high eccentricity to become an EMRI. On the right side, we consider the same system, only this time we arbitrarily increased the relaxation timescale to 4.3×10^{11} yr (by assuming scatter masses of $5 \times 10^{-3} M_\odot$). As depicted this system qualitatively follows the EKL (+GR) behavior.

the small changes in the orbit's energy and angular momentum can cause a change in the angular momentum of about 10%–15%, the effects on EKL are substantial.

For comparison, we consider the same system in Figure 2 (right column), only this time we artificially increased the relaxation timescale, for illustration purposes. In this example, $t_{\text{relx}} \approx 4.3 \times 10^{11}$ yr, which is also longer than the lifetime of the system, and the BH simply undergoes diffusion. As clearly depicted in the figure, the diffusion in this system is insignificant and does not trigger larger EKL effects. Furthermore, in this example, we find that $h/\Delta h|_{\text{relx}} \approx 700 \times h/\Delta h|_{\text{EKL}}$. Thus, the relaxation effects, according to this comparison, result in a negligible change. In this panel, we again overplot the two-body relaxation-only effect (+1pN), as shown by the thick red lines. Note that the apparent drift in ω , in this case, is due to the 1pN precession; a similar drift is depicted in the left column, only modulated by the diffusion processes.

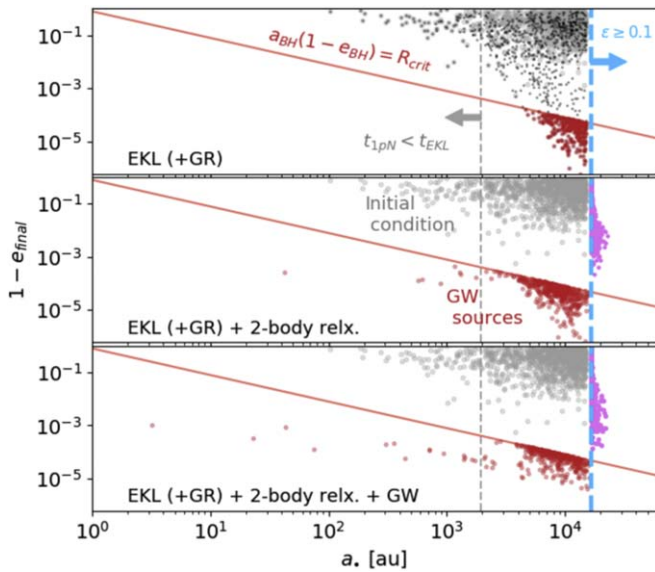


Figure 3. Monte Carlo. As a proof of concept, we consider a system composed of $m_1 = 10^7 M_\odot$ and $m_2 = 10^9 M_\odot$ with a binary separation of $a_{\text{bin}} = 1$ pc and eccentricity of $e_{\text{bin}} = 0.7$. We present three runs, of 1000 particles each. We consider the following processes: (top) EKL + GR, (middle) EKL + GR + two-body relaxation, (bottom) EKL + GR + two-body relaxation + GW. The initial conditions are the same at each run and are shown in gray in each panel. The red line marks the limit of crossing R_{crit} , thus a system that ended up below the line is marked as a potential GW source, i.e., EMRI.

As depicted in the bottom two panels in Figure 3, the nominal suppression of eccentricity excitations due to 1pN precession does not take place. To guide the eye we have outlined the $t_{\text{EKL}} = t_{1\text{pN}}$ line for $e_* = 2/3$. Indeed, without two-body relaxation processes, eccentricity excitations are suppressed in the presence of GR precession (e.g., Ford et al. 2000; Naoz et al. 2013b). However, the small kicks result in a diffusion, thus allowing the eccentricity excitation to take place over a wide range of the parameter space.

Lastly, a striking feature of Figure 2 is that in the presence of two-body relaxation the system moves in and out libration regime, not in sync with EKL. The resonant angle, ω , is known to change from libration to circulation in EKL (e.g., Li et al. 2014a; Hansen & Naoz 2020). However, as depicted, the diffusion process changes these processes, even when the two-body relaxation effects are insignificant. These small kicks allow the (already chaotic) system to transfer zones.

3.2. Monte Carlo Proof of Concept

As mentioned, two-body relaxation processes are often ignored when analyzing the EKL-like systems. On the other hand, EKL is often ignored when considering objects sinking into an SMBH. Here, we qualitatively show the importance of combining these two processes. We consider the system highlighted in Figure 1, of $m_1 = 10^7 M_\odot$ and $m_2 = 10^9 M_\odot$ with a binary separation of $a_{\text{bin}} = 1$ pc and eccentricity of $e_{\text{bin}} = 0.7$. We populate the area of m_1 with 1000 stellar-mass BHs, adopting a Bahcall & Wolf (1976) distribution, i.e., $\alpha = 7/4$, profile. We also adopt a thermal distribution for the stellar-mass BHs and a mutual inclination that is taken from isotropic distribution (i.e., uniform in $\cos i$). The argument of periapsis and the longitude of ascending nodes are taken from a uniform distribution between 0 and 2π .

In Figure 3 we present the results of three sets of simulations of 10^3 particles each, while adopting the following physical processes (top) EKL + GR, (middle) EKL + GR + two-body relaxation, (bottom) EKL + GR + two-body relaxation + GW. The light-gray point in each panel represents the initial conditions (which are identical in each panel). We have three stopping conditions:

1. The simulation reaches 10^9 yr (depicted as black small points). This result only happens in the EKL + GR run (top panel), where about 69% of the systems have survived throughout the EKL + GR simulation (this is consistent with the results for dark matter particles by Naoz & Silk 2014).
2. The stellar-mass BH pericenter crossed a critical distance, which we adopt as $R_{\text{sch}} = 8Gm_1/c^2$, (following Naoz & Silk 2014; Naoz et al. 2019), which is inside the Kerr BH’s innermost retrograde stable orbit. These are represented by red points below the solid line. We label them as “GW sources.” In the EKL + GR, about 31% of all systems crossed the critical radius, while 50% (53%) of all systems in the EKL + GR + two-body relaxation (+GW) run have ended up as GW sources.
3. The BH semimajor axis changed due to two-body relaxation such that $\epsilon > 0.1$ (pink points, to the right of the dashed line). This is only possible when the two-body relaxation is turned on.

While it is clear that the systems whose pericenter crossed R_{sc} are GW sources (i.e., EMRI candidates), it may be less obvious to understand what is the outcome of those with $\epsilon > 0.1$. We emphasize that this condition for hierarchy is based on the octupole prefactor and therefore is somewhat arbitrary (e.g., Lithwick & Naoz 2011). Furthermore, it was suggested in Bhaskar et al. (2021) that violating this role often results in even higher eccentricities. Thus, we refer to those systems as possible EMRI candidates as well.⁹ We find that between $\approx 50\%$ and 100% of the BHs (corresponding to a pericenter smaller than R_{crit} , to $\epsilon > 0.1$) become a GW source.

For pericenters smaller than R_{crit} , Kerr geometry may cause the BHs to spend a lot of time on the SMBH’s ergosphere (Schnittman 2015) where GW emission may shrink their separations. Furthermore, special relativity effects should also be taken into account (Yunes et al. 2008; Berry & Gair 2013).

As can be seen from Figure 3, the combination of EKL with two-body relaxation allows the system to access a larger part of the parameter space, thus triggering the EKL mechanism. In general, the number of objects that undergo high-eccentricity excitation depends on the density distribution (e.g., Li et al. 2015; B. Mockler et al. 2022, in preparation). Moreover, because the two-body relaxation timescale is highly sensitive to the density profile (i.e., α ; see, for example, Figure 1 in Rose et al. 2020), we expect that the efficiency of the combined

⁹ Note that systems that crossed the Roche limit (or the Hill sphere) of the secondary may also be considered as systems that descend toward the SMBH (either the primary or secondary) following Chen et al. (2008, 2009, 2011). Similar arguments were done for systems for which $\epsilon > 0.1$ (e.g., Bhaskar et al. 2021). Furthermore, E. Zhang et al. (2022, in preparation) showed that even in the case of this Roche limit crossing of a tertiary, the system may not change its energy or angular momentum at the order of itself for long timescales. In other words, the system may still be considered “stable” and the eccentricity may continue to increase via EKL. Thus, the combined effect of EKL + two-body relaxation processes may continue to occur for BHs for which $\epsilon > 0.1$, until resulting in possible EMRIs (see Appendix B).

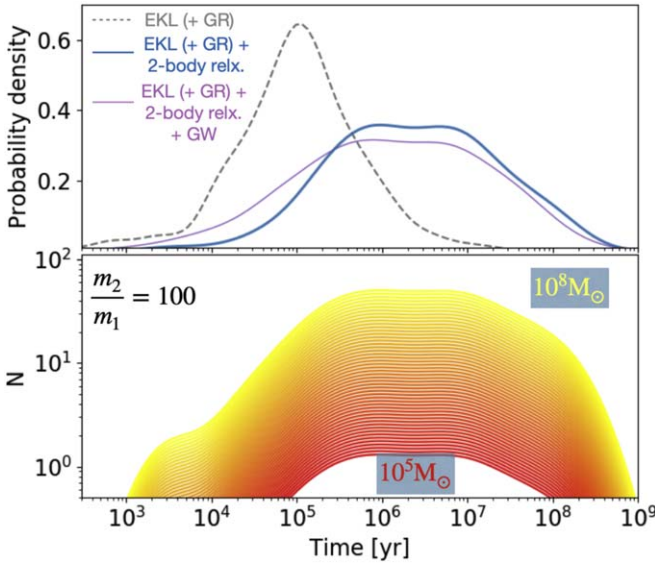


Figure 4. Scaling relation proof of concept. The top panel shows the probability density of the BHs that cross R_{crit} and thus become a GW source, as a function of time, in each of the three simulations from Figure 3. Note that the statistical difference between the two probability densities that include the two-body relaxation is negligible. In particular, the two-sample Kolmogorov–Smirnov test does not reject the null hypothesis—that both have the same distribution—at the 20% significance level. The bottom panel shows the number of stellar-mass BHs that became GW sources as a function of time, for a range of primary masses between 10^5 and $10^8 M_{\odot}$ (from bottom to top). In generating this estimate we have assumed a constant t_{EKL} , constant mass ratio, and that the maximum distance for stellar-mass BHs corresponds to $\epsilon = 0.1$; see Equation (10). We estimate the number of stellar-mass BHs using the M – σ relation (see the text for more details).

system will depend on the underlying density distribution (see D. Melchor et al. 2022, in preparation).

4. EMRI Rate Estimation

The rate estimation is very sensitive to the steady-state number of BHs around the SMBH. It varies over three orders of magnitude between the various assumptions for EMRI formation processes (e.g., Freitag 2001; Hopman & Alexander 2005; Hopman 2009; Amaro-Seoane & Preto 2011; Aharon & Perets 2016; Bar-Or & Alexander 2016; Babak et al. 2017). Thus, here we aim to highlight the efficiency of the proposed mechanism by utilizing the M – σ relation for the number of BHs. We then compare similar approaches in the literature for the two-body relaxation process.

The EKL-only runs compared to the ones with two-body relaxation processes yield a significantly different flux of GW source formation. This is shown in the top panel of Figure 4, where a striking feature is the EKL (+GR)-only result. This feature is consistent with a “burst”-like behavior that depletes the stellar-mass BHs, which could otherwise become GW sources (a similar behavior was found for tidal disruption events (TDEs) and dark matter particle depletion; Naoz & Silk 2014; Li et al. 2015). Thus, for a relatively short time (6×10^5 yr, corresponding to the width of the distribution), the rate is high, but on the timescale it takes to replenish the stellar-mass BH population, the rate is low. Replenishment of BHs can take place via mass segregation, which brings BHs in from the sphere of influence (e.g., Hopman & Alexander 2006). The corresponding timescale is at the order of the two-body relaxation timescale up to a factor of the mass ratio between the

BHs and the stars. Another source of replenishment is star formation, which for our galactic center is estimated to occur every few $\times 10^6$ yr (Lu et al. 2013). Unlike the EKL (+GR)-only result, the inclusion of two-body relaxation expands the timescales at which GW sources can form, thus allowing for the replenishment of stellar-mass BHs to take place.¹⁰

To estimate the number of BHs, $n_{\text{BH}}(\leq r_*)$, within a distance r_{max} we use the M – σ relation:

$$\begin{aligned} n_{\text{BH}}(\leq r_{\text{max}}) &= f_{\text{BH}} \frac{M(\leq r_{\text{max}})}{\langle m_{\star} \rangle} \\ &= 2f_{\text{BH}} \frac{m_1}{\langle m_{\star} \rangle} \left(\frac{G\sqrt{m_1 M_0}}{\sigma_0^2 r_*} \right)^{-3+\alpha}, \end{aligned} \quad (11)$$

where $M(\leq r_{\text{max}}) = \int_0^{r_{\text{max}}} \rho(r') 4\pi r'^2 dr'$ and ρ is the density profile from Equation (1). Furthermore, $\langle m_{\star} \rangle$ is the average mass of the stars and f_{BH} is the fraction of BHs from the overall stellar population, where we adopt $f_{\text{BH}} = 3.2 \times 10^{-3}$ (e.g., Aharon & Perets 2016). In our fiducial system, $r_{\text{max}} = 0.07$ pc, which corresponds to $\epsilon = 0.1$, and the number of BHs within this radius is about 330.

As highlighted in previous studies, it is straightforward to scale the system to a wide range of primary masses, for a constant mass ratio, while holding the quadrupole timescale (Equation (2)) constant¹¹ and considering the number of BHs up to r_{max} , for $\epsilon = 0.1$, (e.g., Naoz & Silk 2014; Naoz et al. 2019). Thus, in Figure 4, bottom panel, we show the number of stellar-mass BHs that are sunk into the SMBH, for the run that includes all of the aforementioned physical processes. In this scaling proof of concept, r_{max} is then mass dependent, and it takes the following form:

$$\begin{aligned} r_{\text{max}} &= \left(\frac{15}{16} \right)^{2/3} t_{\text{EKL}}^{2/3} q^{-2/3} \left(\frac{\epsilon}{e_{\text{bin}}} \right)^2 (1 - e_{\text{bin}}^2) (Gm_1)^{1/3} \\ &\approx 0.07 \text{ pc} \left(\frac{t_{\text{EKL}}}{930 \text{ yr}} \right)^{2/3} \left(\frac{q}{0.01} \right)^{-2/3} \left(\frac{\epsilon}{0.1} \right)^2 \\ &\quad \times \left(\frac{e_{\text{bin}}}{0.7} \right)^2 \left(1 - \left[\frac{e_{\text{bin}}}{0.7} \right]^2 \right) \left(\frac{m_1}{10^7 M_{\odot}} \right), \end{aligned} \quad (12)$$

where $q = m_1/m_2$ is the mass ratio. We note that both in Figure 3 and below we refer to these objects as GW sources and EMRIs.

The EMRI rate is then estimated by

$$\Gamma \approx \Gamma_{\text{EKL}} \times f_{\text{EKL}} \times f_{\text{EMRI}} \times n_{\text{BH}}(\leq r_{\text{max}}), \quad (13)$$

where f_{EMRI} is the fraction of systems that may become an EMRI rather than a plunged orbit, f_{EKL} is the fraction of systems that have their eccentricity excited to cross R_{sch} , and Γ_{EKL} is the rate estimated in the simulation. We estimate the latter by calculating the average accretion time and estimating $\pm 68\%$ of it from our fiducial simulations (i.e., taking 1σ of the accretion time, estimated from Figure 4) and normalized to the range of primary masses as described above (see Figure 4,

¹⁰ Note that in these cases, during the long timescales, the SMBH binary’s separation is expected to shrink, yielding an enhancement of the EMRI rate (e.g., Iwasa & Seto 2016). The inclusion of this effect is beyond the scope of this paper.

¹¹ Note that we limit our analysis to systems for which $t_{\text{EKL}} < t_{\text{relx}}$, to allow for the behavior outlined in Figure 3 to take place.

bottom panel). As highlighted in Figure 3, a large fraction of systems sink into the SMBH when both EKL and two-body relaxation operate, i.e., $f_{\text{EKL}} \sim 0.5-1$.

In Appendix B, we estimate the fraction of systems that are likely to appear within the LISA band (f_{EMRI}). Roughly speaking, one divides between plunging orbits, which may be characterized with a short GW burst, and EMRIs that have many to a few cycles before merging with the SMBH (e.g., Rubbo et al. 2006; Yunes et al. 2008; Berry & Gair 2013, for further discussion). In the former case, special relativity correction may need to be included (e.g., Yunes et al. 2008). Additionally, we note that the pN treatment utilized here may break down around a rotating SMBH because the stellar-mass BHs are expected to spend a lot of time close to the SMBH’s ergosphere before continuing on their original trajectory (Schnittman 2015). Thus, GW emission may alter their orbit. Therefore, the distinction between plunging and cycling orbit represents a large problem in this field.

Based on the above distinction (see Appendix B for more details), we find that about 40% of the systems may be defined as EMRIs. In Appendix B we also present the possible signal-to-noise ratio (S/N) of an example system. Note that the fraction of systems that may end up in the LISA band may depend on the distance of the source.

Using our scaling relation and the number of BHs from Equation (11), the rate is proportional to the mass of the SMBH primary in the following way:

$$\Gamma \approx \Gamma_{\text{EKL}} \times f_{\text{EKL}} \times f_{\text{EMRI}} \times 2f_{\text{BH}} \times m_1^{(3+\alpha)/6} \times \left(\frac{(e_{\text{bin}}/\epsilon)^2 G^{2/3} M_0^{1/2}}{1 - e_{\text{bin}}^2 \sigma_0^2} \right)^{-3+\alpha} \left(\frac{15 \times t_{\text{EKL}}}{16q} \right)^{2(3-\alpha)/3}. \quad (14)$$

Thus, for the scaling relation chosen in this proof of concept, where $\alpha = 7/4$, $q = 0.01$, $e_2 = 0.7$, and t_{EKL} are constant, the rate is proportional to $m_1^{7/8}$. We show this rate in Figure 5 as the shaded band for the following limits: $f_{\text{EKL}} \times f_{\text{EMRI}} = 1-0.2$, where f_{EKL} corresponds to having 50% (100%) from the total number of available BHs become EMRIs and $f_{\text{EMRI}} = 1-0.4$ (see Appendix B).

We also depict the EKL (+GR)-only case during the burst (thin dashed line) and the average over the replenishment time, taken to be a few $\times 10^7$ yr. The EKL (+GR)-only scenario may represent a shallow density distribution ($\alpha \approx 1$) for the BHs, where the two-body relaxation effect is longer and thus can be ignored. However, the density distribution of BHs is expected to be steep (e.g., Bahcall & Wolf 1976) and, therefore, as highlighted here, two-body relaxation processes cannot be ignored. We thus predict the shaded band to be the rate from an SMBH binary.

For comparison, we examine the EMRI rate due only to two-body relaxation. For consistent comparison, we only consider the rate due to the “available” BHs up to r_{max} (i.e., $n_{\text{BH}}(\leq r_{\text{max}})$; Equation (11)). The rate is proportional to the number of BHs over the two-body relaxation timescale. However, as highlighted by Hopman & Alexander (2005), the onset of GW dissipation does not necessarily correspond to the emission of detectable GW emission. Thus, following Hopman & Alexander (2005, Equation (31)) we write the two-body

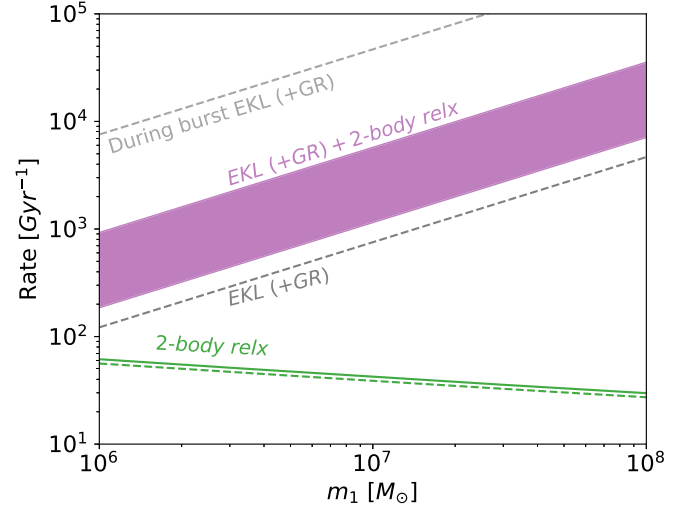


Figure 5. A comparison of the EMRI formation rate for a consistent number of BHs. We consider the case that includes the EKL (+GR) + two-body relaxation estimated rate from Equation (14). We compare it to the EKL (+GR)-only runs, which we consider during the burst (thin dashed line) and over sufficient replenishment time (thick dashed line). The latter is loosely estimated by assuming star formation episode and lifetime of stars to be about 50 Myr. Finally, we depict the EMRI rate for the number of BHs limited to r_{max} (sphere of influence), shown as a dashed (solid) line.

relaxation EMRI rate as

$$\Gamma_{\text{relx}}(\leq r_{\text{max}}) \approx \frac{n_{\text{BH}}}{t_{\text{relx}}(r_{\text{max}}) \ln \delta J} \left(\frac{a_c}{r_{\text{max}}} \right)^{9/2-2\alpha}, \quad (15)$$

where δJ is the ratio of the maximal circular angular momentum at a_c , compared to the angular momentum at the loss cone. Finally, a_c is the critical semimajor axis at which the angular momentum relaxation time is equal to the GW emission decay time (Hopman & Alexander 2005):

$$a_c = r \left(\frac{85}{3072} \right)^{1/(3-\alpha)} \left[\frac{1}{r} \left(\frac{G m_{\text{BH}} t_{\text{relx}}}{\sqrt{GM}} \right)^{2/3} \right]^{3/(6-2\alpha)}, \quad (16)$$

where for consistency we evaluate this critical value at r_{max} (as well as t_{relx}), but in the literature this and the rate from Equation (15) are evaluated at the sphere of influence. Regardless of the distance we choose (i.e., either r_{max} or the sphere of influence), the rate depends on the SMBH mass weakly: $\Gamma_{\text{relx}} \approx m_1^{-1/4}$, (e.g., Hopman & Alexander 2005). In Figure 5, we show this rate for r_{max} (the sphere of influence), dashed (solid) line.

5. Discussion

EMRIs are the result of an SMBH that captures a stellar-mass compact object, such as a BH. Thus, these are some of the promising GW signals for low-frequency GW detectors such as LISA. Different channels have been suggested to form EMRIs. In particular, two-body relaxation has been proposed as one of the likely physical processes to form EMRIs efficiently. In this process, weak two-body kicks from the population of stars and compact objects that surrounds the SMBH can change the BH’s orbit over time, driving it into the SMBH. On the other hand, perturbations from SMBH companions, via the EKL mechanism, can excite the SMBH to high eccentricities, thereby forming EMRIs. Here we demonstrated that EMRIs are

naturally formed in SMBH binaries with higher efficiency than either of these processes considered alone.

In the presence of an SMBH companion, the EKL mechanism can excite the BH's eccentricity to high values. However, the EKL mechanism's efficiency depends to some extent on the initial conditions (e.g., Li et al. 2014a). Therefore, the small kicks due to two-body relaxation do not need to accumulate to change the angular momentum by an order of itself. Instead, they can change the orbital parameters of the stellar-mass BH, such as eccentricity, semimajor axis, and argument of periapsis, rendering it in a favorable EKL regime. We show an example of such a system in Figure 2. Even if the two-body relaxation timescale is orders of magnitude longer than the EKL timescale (see Figure 1), the small kicks are effective as long as they result in a change of angular momentum comparable to that due to EKL. In particular, we suggest that $h/\Delta h|_{\text{relx}}$ needs to be within a couple of orders of magnitude of (or close to) $h/\Delta h|_{\text{EKL}}$. If $h/\Delta h|_{\text{relx}} \gg h/\Delta h|_{\text{EKL}}$, the angular momentum change Δh due to the two-body relaxation can be ignored (see, for example, Figure 2). In Figure 1 we highlight the proposed comparison between the two-body relaxation process and EKL, using $h/\Delta h$ rather than timescales.

In general, other collective processes may also be considered. For example, resonant relaxations (Rauch & Tremaine 1996), which arise from the orbit-averaged mass distribution of the objects around the primary, can be added as well (e.g., Eilon et al. 2009; Kocsis & Tremaine 2011; Sridhar & Touma 2016; Touma et al. 2019). However, scalar and vector resonant relaxation processes modify the angular momentum $\Delta h/h_{\text{RR}} \sim t_{\text{res}}/P$, thus using their timescales to estimate their contribution may not be as misleading as the aforementioned timescale analysis of the two-body relaxation (instead of using $\Delta h/h$). Vector resonant relaxation processes have been added recently to the EKL context and were shown to drive low-inclination configurations to a more EKL-favorable regime (e.g., Hamers et al. 2018). However, the latter study concluded that overall, the combined effect is not very efficient in the context of BH–BH mergers. In contrast, as highlighted here, two-body relaxation results in populating EKL-favorable regimes very efficiently.

As a proof of concept, we choose a fiducial system composed of an SMBH binary ($m_1 = 10^7 M_\odot$, and $m_2 = 10^9 M_\odot$) on an eccentric orbit $e_{\text{bin}} = 0.7$, at 1 pc separation. We begin by considering the effect of the EKL mechanism on stellar-mass BHs around m_1 (Figure 3 top panel). Note that all runs include the 1pN contribution to the inner and outer orbits.¹² Stellar-mass BHs whose pericenter distance passed a critical value are considered as EMRIs. As noted in previous studies, the efficacy of this mechanism is about 30% (e.g., Naoz & Silk 2014). We then systematically add two-body relaxation (middle panel in Figure 3) and GW emission (bottom panel). As a result, the efficacy increased to 50%–100%, meaning nearly all of the stellar-mass BHs ended up descending into the SMBH, thereby possibly forming EMRIs, within a few $\times 10^8$ yr, after a single star formation burst, i.e., not including replenishment.

To highlight the efficiency of this scenario, we extrapolate the EMRI formation rate to different SMBHs. Because the EMRI rate is highly uncertain and is sensitive to the number of

BHs as a function of time, we used the M – σ relation. Moreover, we rescale our fiducial example by keeping the quadrupole level of the EKL approximation constant. This means a constant power law and a constant mass ratio, and the SMBH binary separation varies accordingly, for example, for $m_1 = 10^7 M_\odot$ ($m_1 = 10^8 M_\odot$) and $a_{\text{bin}} = 1$ pc ($a_{\text{bin}} = 2.2$ pc). Furthermore, the number of BHs inside a sphere at which $\epsilon \leq 0.1$ varies accordingly, for $m_1 = 10^7 M_\odot$ ($m_1 = 10^8 M_\odot$) and $N_{\text{BH}} \approx 331$ ($N_{\text{BH}} \sim 1979$). We depict the rescaling in Figure 4.

Even for this simple scaling, it is clear that having the entire population of BHs, (or even just 50%) become EMRIs has large implications on the EMRI rate. We compare the predicted EMRI rate from this scenario to the prediction from only two-body relaxation in Figure 5. As depicted in this figure, the EMRI rate in SMBH binaries is orders of magnitude larger than that in isolated SMBHs. Additionally, the dependence on the SMBH mass is different, offering a potential way to disentangle between the different scenarios. Furthermore, because SMBH binaries are expected to be ubiquitous in the universe, our results suggest that the EMRI rate may be much higher than nominal estimations. In particular, post-starburst galaxies may be interesting candidates for enhanced EMRI formation as they possibly host an SMBH binary. Moreover, this result suggests that the observed EMRI rate may be used to constrain the prevalence of SMBH binaries in the universe.

We thank the referee for useful comments. S.N. acknowledges the partial support from NASA ATP 80NSSC20K0505 and thanks Howard and Astrid Preston for their generous support. S.R. thanks the Nina Byers Fellowship, the Charles E. Young Fellowship, and the Michael A. Jura Memorial Graduate Award for support, as well as partial support from NASA ATP 80NSSC20K0505. E.M. acknowledges the support from Howard and Astrid Preston, the Mani L. Bhaumik Institute for Theoretical Physics, and as well as partial support from NASA ATP 80NSSC20K0505. D.M. acknowledges partial support from an NSF graduate fellowship DGE-2034835, the Eugene Cota-Robles Fellowship, and NASA ATP 80NSSC20K0505. B.M. is grateful for the AAUW American Fellowship, and the UCSC President's Dissertation Fellowship. E.R.-R. and B.M. are grateful for support from the Packard Foundation, Heising-Simons Foundation, NSF (AST-1615881, AST-1911206, and AST-1852393), Swift (80NSSC21K1409, 80NSSC19K1391), and Chandra (GO9-20122X).

Appendix A The Postkick Orbital Parameters

Consider a BH orbiting an SMBH. In the plane of the ellipse, we can define the separation vector as $\mathbf{r} = r(\cos f, \sin f, 0)$, where f is the true anomaly and

$$r = \frac{a(1 - e^2)}{1 + e \cos f}. \quad (\text{A1})$$

The associated velocity vector at the plane of the ellipse is $\mathbf{v} = h/a(-\sin f, e + \cos f, 0)/(1 - e^2)$. These vectors are projected onto the invariable plane, wherein the case of a test particle EKL is simply the plane of the outer orbit (e.g., Lithwick & Naoz 2011). Thus, we rotate the separation and velocity vectors at each time step given their argument of

¹² Note that we do not include crossing terms (e.g., Naoz et al. 2013b; Lim & Rodriguez 2020) because their overall effect should be minimal in this configuration.

periapsis ω , longitude of ascending nodes Ω , and inclination i . For example, and similarly for the velocity vector, we have

$$\mathbf{r}_{,\text{inv}} = R_z(\Omega)R_x(i)R_z(\omega)\mathbf{r}_{,\text{ell}}, \quad (\text{A2})$$

where the subscripts ‘‘inv’’ and ‘‘ell’’ refer to the invariable and ellipse coordinate systems, respectively. Given a rotation angle θ , the rotation matrices R_z and R_x are

$$R_z(\theta) = \begin{pmatrix} \cos \theta & -\sin \theta & 0 \\ \sin \theta & \cos \theta & 0 \\ 0 & 0 & 1 \end{pmatrix} \quad (\text{A3})$$

and

$$R_x(\theta) = \begin{pmatrix} 1 & 0 & 0 \\ 0 & \cos \theta & -\sin \theta \\ 0 & \sin \theta & \cos \theta \end{pmatrix}. \quad (\text{A4})$$

A two-body encounter can change its velocity by

$$\Delta v = v_* \sqrt{\frac{P}{t_{\text{relx}}}}. \quad (\text{A5})$$

We model this change as a random walk, applying a single isotropic, instantaneous, kick to the BH velocity once per P . Each directional component of this 3D kick is drawn from a Gaussian distribution with a zero average and a standard deviation of $\Delta v_j/\sqrt{3}$, where j is 1, 2, and 3 for the three components of the velocity vector. The instantaneous assumption means that r_* is kept constant during the kick (see Kalogera 2000).

Thus, post-kick, the new velocity vector (in the invariable plane) is $\mathbf{v}_{*,p} = \Delta v + \mathbf{v}_*$, where we dropped the subscript ‘‘inv’’ to avoid clutter and the subscript ‘‘p’’ means post-kick. The angular momentum postkick is $\mathbf{h}_p = \mathbf{r}_* \times \mathbf{v}_{*,p}$. Thus, it is straightforward to find the orbital parameters. Specifically, the semimajor axis of the BH post-kick is

$$a_{*,p} = \left(\frac{2}{r_*} - \frac{v_{*,p}^2}{Gm_1} \right)^{-1}, \quad (\text{A6})$$

the post-kick eccentricity is

$$e_{*,p} = \sqrt{1 - \frac{h_p^2}{Gm_1 a_{*,p}}}. \quad (\text{A7})$$

Because the z -axis is defined by the outer orbit, the new inclination is $\cos i_p = h_{p,z}/h_p$, where $h_{p,z}$ is the z component of the post-kick angular momentum.

The post-kick longitude of ascending nodes is

$$\Omega_p = \arctan_2 \left(\pm \frac{h_{p,1}}{h_p \sin i_p}, \mp \frac{h_{p,2}}{h_p \sin i_p} \right). \quad (\text{A8})$$

The post-kick true anomaly is

$$f_p = \arctan_2 \left(\frac{a_{*,p}(1 - e_{*,p}^2)}{h_p e_{*,p}} \dot{R}_p, \times \frac{1}{e_{*,p}} \left[\frac{a_{*,p}(1 - e_{*,p}^2)}{r_*} - 1 \right] \right), \quad (\text{A9})$$

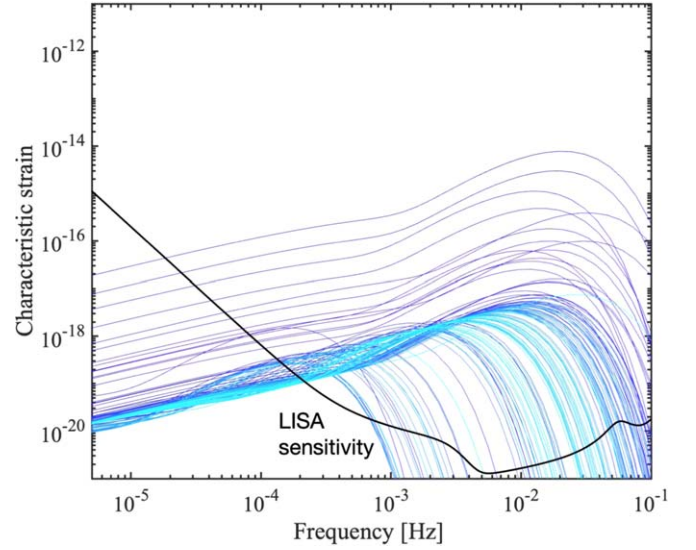


Figure 6. An example of the characteristic strain for 150 (chosen randomly) of the runs that reached $P_* \leq 10$ yr and $a_*(1 - e_*) < 1$ au. We consider the case that includes EKL (+GR) + two-body relaxation + GW.

where $\dot{R} = \pm \sqrt{v_{*,p}^2 - h_p^2/r_*^2}$, where the sign is defined by the sign of $\mathbf{r}_* \cdot \mathbf{v}_{*,p}$ (e.g., Murray & Dermott 2000). The post-kick argument of pericenter is then

$$\omega_p = \arctan_2 \left(\frac{r_{*,3}}{r_* \sin i_p}, \left[\frac{r_{*,1}}{r_*} + \frac{r_{*,3} \sin \omega_p \cos i_p}{r_* \sin i_p} \right] \sec \Omega_p \right) - f_p, \quad (\text{A10})$$

Appendix B Plunging Orbits and an Example of Signal-to-Noise Ratio in the LISA Band


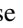


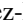

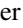
We first differentiate between plunging orbits and EMRIs, where the former is described as a burst associated with their pericenter passage. Our adopted stopping condition of $R_{\text{sch}} = 8Gm_1/c^2$ means that beyond this threshold the BH trajectory will be modified by Kerr geometry and special relativity (e.g., Yunes et al. 2008; Berry & Gair 2013; Schnittman 2015; Schnittman et al. 2018). The specific trajectories are beyond the scope of this study. Nonetheless, in the presence of GW emission, we can roughly estimate the fraction of systems that are more likely to appear as EMRIs rather than GW bursts. For that, we first confirmed that all of the systems in the EKL (+GR) + two-body relaxation indeed reach the Schwarzschild radius by integrating all of the systems below the solid line in the bottom panel of Figure 3.

Second, examining the integration prior to the threshold we found that $\sim 40\%$ of the system reach a configuration for which $P_* \leq 10$ yr and $a_*(1 - e_*) < 1$ au. This specific configuration is chosen such that the characteristic strain will appear in the LISA band, resulting in millihertz signals (see below). Assuming the LISA lifetime to be about 10 yr. We emphasize that the 40% estimation is rather conservative because, as mentioned, even the plunged BHs’ trajectories may spend a long time zooming in the SMBH’s ergosphere, where GW emission may alter their separation and can result in an EMRI-like signal. Note that even when the BH period is smaller than

10 yr (roughly equivalent to S0-2's orbital period), two-body relaxation may still result in small kicks, about 0.0003 of the BH velocity, according to Equation (8). Thus, overall the orbit will not substantially change over the BH period.¹³

To estimate the signal to noise, we follow Robson et al. (2019a, 2019b). The strain and thus the S/N depend on the orbital period, the eccentricity, and the luminosity distance. As a proof of concept, we depict in Figure 6 the characteristic strain for all of the runs that crossed R_{sch} in our nominal system (i.e., all the points below the line in Figure 3). For this example, we adopt a luminosity distance of 0.7 Mpc, and LISA observation time of 10 yr. We find that 52% of the systems have an $S/N > 5$. Out of these systems, 3% have a GW dissipation timescale shorter than 10 yr, which implies that a more careful analysis of the characteristic strain should be conducted for them (e.g., Barack & Cutler 2004). Eccentricity oscillations due to the EKL signature on the characteristic strain (e.g., Hoang et al. 2019; Deme et al. 2020) are unlikely to be detected in this configuration.

ORCID iDs

Smadar Naoz  <https://orcid.org/0000-0002-9802-9279>
 Sanaea C. Rose  <https://orcid.org/0000-0003-0984-4456>
 Erez Michaely  <https://orcid.org/0000-0002-9705-8596>
 Denyz Melchor  <https://orcid.org/0000-0002-7854-1953>
 Enrico Ramirez-Ruiz  <https://orcid.org/0000-0003-2558-3102>
 Brenna Mockler  <https://orcid.org/0000-0001-6350-8168>
 Jeremy D. Schnittman  <https://orcid.org/0000-0002-2942-8399>

References

- Aharon, D., & Perets, H. B. 2016, *ApJL*, 830, L1
 Alexander, T., & Hopman, C. 2009, *ApJ*, 697, 1861
 Amaro-Seoane, P. 2018, *LRR*, 21, 4
 Amaro-Seoane, P., & Preto, M. 2011, *CQGra*, 28, 094017
 Amaro-Seoane, P., Audley, H., Babak, S., et al. 2017, arXiv:1702.00786
 Antognini, J. M. O. 2015, *MNRAS*, 452, 3610
 Babak, S., Gair, J., Sesana, A., et al. 2017, *PhRvD*, 95, 103012
 Bahcall, J. N., & Wolf, R. A. 1976, *ApJ*, 209, 214
 Baker, J., et al. 2019, arXiv:1907.06482
 Barack, L., & Cutler, C. 2004, *PhRvD*, 69, 082005
 Bar-Or, B., & Alexander, T. 2016, *ApJ*, 820, 129
 Batcheldor, D., Robinson, A., Axon, D. J., Perlman, E. S., & Merritt, D. 2010, *ApJL*, 717, L6
 Berry, C. P. L., & Gair, J. R. 2013, *MNRAS*, 433, 3572
 Bhaskar, H., Li, G., Hadden, S., Payne, M. J., & Holman, M. J. 2021, *AJ*, 161, 48
 Bianchi, S., Chiaberge, M., Piconcelli, E., Guainazzi, M., & Matt, G. 2008, *MNRAS*, 386, 105
 Binney, J., & Tremaine, S. 2008, *Galactic Dynamics* (2nd ed.; Princeton, NJ: Princeton Univ. Press)
 Blaes, O., Lee, M. H., & Socrates, A. 2002, *ApJ*, 578, 775
 Bode, J. N., & Wegg, C. 2014, *MNRAS*, 438, 573
 Bogdanović, T., Eracleous, M., & Sigurdsson, S. 2009, *ApJ*, 697, 288
 Boroson, T. A., & Lauer, T. R. 2009, *Natur*, 458, 53
 Bradnick, B., Mandel, I., & Levin, Y. 2017, *MNRAS*, 469, 2042
 Callegari, S., Mayer, L., Kazantzidis, S., et al. 2009, *ApJL*, 696, L89
 Chen, X., & Han, W.-B. 2018, *CmPhy*, 1, 53
 Chen, X., & Liu, F. K. 2013, *ApJ*, 762, 95
 Chen, X., Liu, F. K., & Magorrian, J. 2008, *ApJ*, 676, 54
 Chen, X., Madau, P., Sesana, A., & Liu, F. K. 2009, *ApJL*, 697, L149
 Chen, X., Sesana, A., Madau, P., & Liu, F. K. 2011, *ApJ*, 729, 13
 Comerford, J. M., Griffith, R. L., Gerke, B. F., et al. 2009, *ApJL*, 702, L82
 Comerford, J. M., Nevin, R., Stemo, A., et al. 2018, *ApJ*, 867, 66
 Deane, R. P., Paragi, Z., Rumsey, C., et al. 2014, *Natur*, 511, 57
 Deme, B., Hoang, B.-M., Naoz, S., & Kocsis, B. 2020, *ApJ*, 901, 125
 Di Matteo, T., Springel, V., & Hernquist, L. 2005, *Natur*, 433, 604
 Dotti, M., Montuori, C., Decarli, R., et al. 2009, *MNRAS*, 398, L73
 Eilon, E., Kupi, G., & Alexander, T. 2009, *ApJ*, 698, 641
 Ford, E. B., Joshi, K. J., Rasio, F. A., & Zbarsky, B. 2000, *ApJ*, 528, 336
 Fragione, G., Loeb, A., Kremer, K., & Rasio, F. A. 2020, *ApJ*, 897, 46
 Freitag, M. 2001, *CQGra*, 18, 4033
 Generozov, A., & Madigan, A.-M. 2020, *ApJ*, 896, 137
 GRAVITY Collaboration et al 2020, *A&A*, 636, L5
 Green, P. J., Myers, A. D., Barkhouse, W. A., et al. 2010, *ApJ*, 710, 1578
 Gualandris, A., & Merritt, D. 2009, *ApJ*, 705, 361
 Gürkan, M. A., & Rasio, F. A. 2005, *ApJ*, 628, 236
 Hamers, A. S., Bar-Or, B., Petrovich, C., & Antonini, F. 2018, *ApJ*, 865, 2
 Hansen, B. M. S., & Milosavljević, M. 2003, *ApJL*, 593, L77
 Hansen, B. M. S., & Naoz, S. 2020, *MNRAS*, 499, 1682
 Haster, C.-J., Antonini, F., Kalogera, V., & Mandel, I. 2016, *ApJ*, 832, 192
 Hoang, B.-M., Naoz, S., Kocsis, B., Farr, W. M., & McIver, J. 2019, *ApJL*, 875, L31
 Hopkins, P. F., Hernquist, L., Cox, T. J., et al. 2006, *ApJS*, 163, 1
 Hopman, C. 2009, *CQGra*, 26, 094028
 Hopman, C., & Alexander, T. 2005, *ApJ*, 629, 362
 Hopman, C., & Alexander, T. 2006, *ApJL*, 645, L133
 Iwasa, M., & Seto, N. 2016, *PhRvD*, 93, 124024
 Kalogera, V. 2000, *ApJ*, 541, 319
 Kocsis, B., & Tremaine, S. 2011, *MNRAS*, 412, 187
 Komossa, S., Burwitz, V., Hasinger, G., et al. 2003, *ApJL*, 582, L15
 Komossa, S., Zhou, H., & Lu, H. 2008, *ApJL*, 678, L81
 Kozai, Y. 1962, *AJ*, 67, 591
 Kremer, K., Lombardi, James, C., et al. 2022, arXiv:2201.12368
 Li, G., Naoz, S., Holman, M., & Loeb, A. 2014a, *ApJ*, 791, 86
 Li, G., Naoz, S., Kocsis, B., & Loeb, A. 2014b, *ApJ*, 785, 116
 Li, G., Naoz, S., Kocsis, B., & Loeb, A. 2015, *MNRAS*, 451, 1341
 Li, K., Bogdanović, T., & Ballantyne, D. R. 2020, *ApJ*, 896, 113
 Lidov, M. L. 1962, *P&SS*, 9, 719
 Lim, H., & Rodriguez, C. L. 2020, *PhRvD*, 102, 064033
 Lithwick, Y., & Naoz, S. 2011, *ApJ*, 742, 94
 Liu, X., Greene, J. E., Shen, Y., & Strauss, M. A. 2010, *ApJL*, 715, L30
 Lu, C. X., & Naoz, S. 2019, *MNRAS*, 484, 1506
 Lu, J. R., Do, T., Ghez, A. M., et al. 2013, *ApJ*, 764, 155
 Maillard, J. P., Paumard, T., Stolovy, S. R., & Rigaut, F. 2004, *A&A*, 423, 155
 McConnell, N. J., & Ma, C.-P. 2013, *ApJ*, 764, 184
 Mei, J., Bai, Y.-Z., Bao, J., et al. 2020, *PTEP*, 2021, 05A107
 Metzger, B. D., Stone, N. C., & Gilbaum, S. 2022, *ApJ*, 926, 101
 Miller, M. C., Freitag, M., Hamilton, D. P., & Lauburg, V. M. 2005, *ApJL*, 631, L117
 Murray, C. D., & Dermott, S. F. (ed.) 2000, *Solar System Dynamics* (Cambridge: Cambridge Univ. Press)
 Naoz, S. 2016, *ARA&A*, 54, 441
 Naoz, S., Farr, W. M., Lithwick, Y., Rasio, F. A., & Teyssandier, J. 2013a, *MNRAS*, 431, 2155
 Naoz, S., Kocsis, B., Loeb, A., & Yunes, N. 2013b, *ApJ*, 773, 187
 Naoz, S., Li, G., Zanardi, M., de Elía, G. C., & Di Sisto, R. P. 2017, *AJ*, 154, 18
 Naoz, S., & Silk, J. 2014, *ApJ*, 795, 102
 Naoz, S., Silk, J., & Schnittman, J. D. 2019, *ApJL*, 885, L35
 Naoz, S., Will, C. M., Ramirez-Ruiz, E., et al. 2020, *ApJL*, 888, L8
 Pan, Z., & Yang, H. 2021, *PhRvD*, 103, 103018
 Pesce, D. W., Braatz, J. A., Condon, J. J., & Greene, J. E. 2018, *ApJ*, 863, 149
 Peters, P. C., & Mathews, J. 1963, *PhRv*, 131, 435
 Preto, M., & Amaro-Seoane, P. 2010, *ApJL*, 708, L42
 Rauch, K. P., & Tremaine, S. 1996, *NewA*, 1, 149
 Raveh, Y., & Perets, H. B. 2021, *MNRAS*, 501, 5012
 Robertson, B., Bullock, J. S., Cox, T. J., et al. 2006, *ApJ*, 645, 986
 Robson, T., Cornish, N., & Liu, C. 2019a, *CQGra*, 36, 105011
 Robson, T., Cornish, N. J., & Liu, C. 2019b, *CQGra*, 36, 105011
 Rodriguez, C., Taylor, G. B., Zavalá, R. T., et al. 2006, *ApJ*, 646, 49
 Rose, S. C., Naoz, S., Gautam, A. K., et al. 2020, *ApJ*, 904, 113
 Rose, S. C., Naoz, S., Sari, R., & Linial, I. 2021, arXiv:2201.00022
 Rubbo, L. J., Holley-Bockelmann, K., & Finn, L. S. 2006, *ApJL*, 649, L25
 Runnøe, J. C., Eracleous, M., Pennell, A., et al. 2017, *MNRAS*, 468, 1683
 Sari, R., & Fragione, G. 2019, *ApJ*, 885, 24
 Schnittman, J. D. 2015, *ApJ*, 806, 264

¹³ Note that we are not taking into account star-BH collisions and tidal interactions that may result in electromagnetic signatures or larger BHs (e.g., Metzger et al. 2022; Rose et al. 2021; Kremer et al. 2022).

- Schnittman, J. D., Dal Canton, T., Camp, J., Tsang, D., & Kelly, B. J. 2018, [ApJ](#), 853, 123
- Sillanpaa, A., Haarala, S., Valtonen, M. J., Sundelius, B., & Byrd, G. G. 1988, [ApJ](#), 325, 628
- Smith, K. L., Shields, G. A., Bonning, E. W., et al. 2010, [ApJ](#), 716, 866
- Sridhar, S., & Touma, J. R. 2016, [MNRAS](#), 458, 4143
- Stemo, A., Comerford, J. M., Barrows, R. S., et al. 2021, [ApJ](#), 923, 36
- Touma, J., Tremaine, S., & Kazandjian, M. 2019, [PhRvL](#), 123, 021103
- Tremaine, S., Gebhardt, K., Bender, R., et al. 2002, [ApJ](#), 574, 740
- van den Bosch, R. C. E. 2016, [ApJ](#), 831, 134
- Will, C. M., & Maitra, M. 2017, [PhRvD](#), 95, 064003
- Yunes, N., Sopuerta, C. F., Rubbo, L. J., & Holley-Bockelmann, K. 2008, [ApJ](#), 675, 604
- Zheng, X., Lin, D. N. C., & Mao, S. 2020, [ApJ](#), 905, 169